Model PEM water electrolyzer cell for studies of periodically alternating drainage/imbibition cycles

Supriya Bhaskaran [a,b,*], Tamara Miličić [b], Tanja Vidaković-Koch [b], Vikranth Kumar Surasani [c], Evangelos Tsotsas [a], Nicole Vorhauer-Huget [a]

[a] Institute of Process Engineering, Otto-von-Guericke University Magdeburg, Universitaetsplatz 2, 39106, Magdeburg, Germany
[b] Max Planck Institute for Dynamics of Complex Technical Systems, Sandtorstraße 1, 39106, Magdeburg, Germany
[c] Department of Chemical Engineering, Birla Institute of Technology and Sciences, Pilani- Hyderabad Campus, Shameerpet, Hyderabad, 500078, India

ARTICLE INFO

ABSTRACT

Investigating the counter-current two-phase flow within the anodic porous transport layer (PTL) of polymer electrolyte membrane water electrolyzers (PEMWEs) is a complex yet intriguing challenge. Until now, the gas-liquid invasion processes inside PTLs are only to a limited extent accessible under operation conditions, usually using sophisticated and expensive optical approaches, i.e., neutron imaging. We propose a model-supported experimental method with a fully operating microfluidic PEMWE, that allows to examine pore-scale oxygen-water distributions at the anode with high spatial and temporal resolution. The microfluidic cell is made of transparent Poly-Methyl-Methacrylate (PMMA), and the PTL is simplified by a quasi-2D pore network (PN) with a uniform pore-throat structure in the first preliminary study. The proposed setup is a significant advancement over previous studies, where gas was only injected at a constant flow rate from a single point. Test cases with current densities of 0.1, 1, and 2 A/cm^2 and water flow rates of 1, 3, 5, and 10 ml/min were realized in the novel setup. We found periodically alternating invasion of oxygen (drainage) and water (imbibition), which were analyzed based on image sequences as well as voltage measurements. The experimental data is additionally supported by pore-scale Lattice Boltzmann (LB) and PN simulations. The preliminary results with the simplified PN structure are used to study the dominating transport mechanisms, revealing that drainage and imbibition occur simultaneously and are affected by evaporation and wetting liquid films formed in sharp pore corners. These phenomena are also expected to occur in more complex PTL structures. The preliminary results can, therefore, be regarded as an important basis for PTL studies, which are structurally more complex.

1. Introduction

Driven by the political and societal endeavors to drastically reduce CO$_2$ emissions, the substitution of fossil fuels by green hydrogen is widely considered [1]. Electrochemical splitting of water inside polymer electrolyte membrane water electrolyzers (PEMWEs) is one possibility for efficient and sustained production of green hydrogen [2,3]. A key aspect of the commercialization of PEMWE is improving its performance at high current densities. Related to this is the requirement for an improved understanding of two-phase counter-current transport phenomena that occur inside the porous transport layers (PTL), especially at the anode side [4,5]. In particular, the accumulation of oxygen inside the porous structures of the anode PTL hinders the reactant from reaching the catalyst layer (CL), increasing the mass transport losses,

which significantly reduces the efficiency of the PEMWE cell, especially at high current densities [6]. Besides mathematical modeling, several experimental techniques have been employed in the past to study this issue. Exemplarily, X-ray micro-computed tomography (μ-CT) was used for structural characterization of PTLs. For example, Schuler et al. [7] and Majasan et al. [8–10] derived porosity and pore size distributions (PSD) of different sintered and felt PTLs from μ-CT image data. Similarly, Zielke et al. [11] used μ-CT to determine microstructural properties as a base for the calculation of water permeability.

As an advancement of imaging with μ-CT, several researchers [12–16] developed in-operando neutron imaging to study the structural dependence of gas-liquid transport inside PTLs. Seweryn et al. [17] used a fully operating PEMWE with a sintered titanium PTL and an active area of 1 cm^2 in their study. They investigated the oxygen-water

---

distributions at 0.1–2.5 A/cm^2. Their data revealed no clear correlation between the phase patterns and current density in the studied range. Lee et al. [18] considered higher current densities, between 2 and 9 A/cm^2, and found a blocking of the CL by the produced gas. In addition to that, Lee et al. [19] and Selamet et al. [4] showed that an increased operating temperature can result in lower liquid saturations.

However, although this long list of examples clearly indicates that μ-CT and neutron imaging are indeed very powerful experimental techniques, the aforementioned structure influence can only, to some extent, be investigated by them because of the very fast dynamics of the process and the impossibility to resolve localized drainage/imbibition events with a high temporal resolution [20,21]. This is problematic for the deep understanding of structure-transport correlations.

Details about the local pore-scale processes are usually obtained by experiments with transparent microfluidic platforms as they enable direct (2D) visualization simply by employing optical cameras, e.g. Refs. [22,23]. Exemplarily, using soft-lithography techniques, Arbabi et al. [22] fabricated a polydimethylsiloxane (PDMS) chip with an irregular PN that captured the structural properties of commercial PTLs (felt, foam, sintered) based on information previously obtained by μ-CT. In a similar set-up with pore sizes of around 67 μm, Lee et al. [23] studied gas pathways percolating the liquid-filled PTL. However, one of the major drawbacks of such studies is the injection of liquid and air with constant flow rates, which simplifies the situation in an actual electrochemical cell where the invasion of the gas phase is coupled to the reaction rate.

To overcome this limitation, we propose a novel experimental setup that combines the concept of microfluidic chips used in previous studies [22–24] with an electrochemically active PEMWE cell. This way, we exploit the advantages of microfluidic devices, namely the optical accessibility and the possibility for direct comparison with simulation results [25–29], furthermore we advance it to enable studies of the dynamic invasion of oxygen in dependence of the operating conditions, similarly as realized in neutron imaging studies.

Major interest in this study concerns the visualization of gas-liquid distributions in single pores under different operation conditions to prove the usability of the novel method in the first step. For this purpose, the current densities were varied between 0.1, 1 and 2 A/cm^2, and the water flow rates were between 1, 3, 5, and 10 ml/min. The evolving oxygen invasion pathways were monitored with a framerate of 50 fps, which was much faster than the drainage of single pores in the studied structure. It is shown that drainage and imbibition of water occurred simultaneously in repeating drainage/imbibition cycles, mostly with constant gas-liquid profiles. The specific characteristics of the cycles, i.e. frequency and amplitude, are shown to be dependent on the process conditions, namely current density and water flow rate. The transient phase distributions obtained by drainage were well replicated by PN and LB simulations. Imbibition, though, is not yet implemented in the available models and remains for future work. Regardless of it, simulations and experiments clearly demonstrated that secondary water transport in thick capillary liquid films can significantly contribute to liquid transport as long as temperatures are kept low enough to avoid evaporation.

2. Experimental methodology

2.1. Experimental design and procedure

The cell design is shown in Fig. 1A. The cell body was made of transparent Poly-Methyl-Methacrylate (PMMA) to allow visualization of the fluid flow. It consisted of two compartments, an anode and a cathode, which are both connected to supply channels and outlet channels. The dimensions of both compartments are 25 mm × 20 mm (length × width), with a channel depth of 2 mm. While a simple square PN, with throats of rectangular cross-section, was realized at the anode side, the cathode side contained no structure. The PN morphology used here is a simplification compared to previous works, where μ-CT image data was used to design the pore structure [22,23]. More specifically, the solid blocks that structured the anode had a size of 2 × 2 × 2 mm^3; the voids between these blocks (i.e. the pores and throats) each had a length of 2 mm and a width of 2 mm, with a very small standard deviation which was in the range of production inaccuracies. In this prototype, the PN structure was prepared by milling of the material. As a result, the inner surface of the device exhibited a higher surface roughness than cells that are usually prepared by other methods, such as chemical wet etching.

The gas phase was generated at an electrochemically activated catalyst-coated membrane (CCM). The CCM (manufactured by Fuel Cell Store, USA) and platinum meshes (340 μm, Alfa Aesar by Thermo Fisher Scientific) were sandwiched between the two compartments. The thickness of the Nafion 115 membrane was 127 μm. At the anode side, iridium ruthenium oxide was used as catalyst with a loading of 3 mg/cm^2, while the catalyst used at the cathode side was platinum black with a loading of 3 mg/cm^2.

Deionized water was supplied by syringe pumps (Aladdin Syringe (AL 4000) with two syringes and flow rates between 0.001 μL/h (0.5 μL syringes) and 7515 mL/h (60 mL syringes) manufactured by World Precision Instruments, Germany) (Fig. 1B). As indicated in Fig. 1 both, anode and cathode, were supplied with water to allow stable pressure conditions inside the whole device. The electrochemical measurements were performed using a potentiostat (Energy Lab XM Potentiostat Galvanostat, AMETEK scientific instruments, USA). A Canon EOS 550D camera was used to capture the oxygen-water distribution at the anode every 0.02 s. The cell was aligned horizontally to avoid an impact of gravitation. In the images presented below, the bottom side refers to the CL and the top side to the flow channel (FC). The flow direction of water inside the FC was from right to left (Fig. 1 and supplementary materials S1–S4).

2.2. Experimental parameters

The cell was operated at room temperature of 25 °C and atmospheric pressure under steady-state conditions during measurements. It is noted,
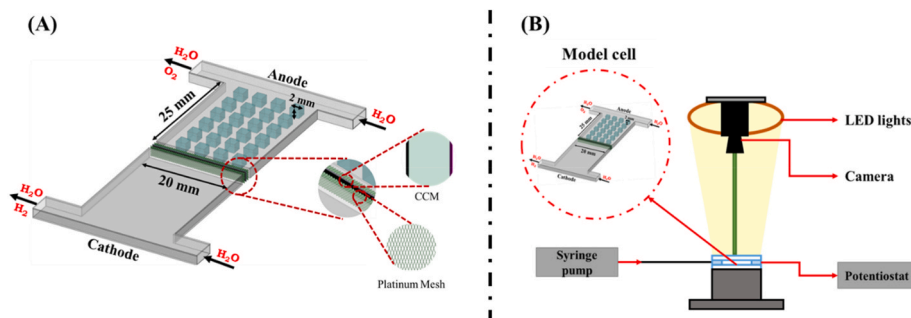

Fig. 1. (A) Schematic representation of the model PEM water electrolyzer cell including dimensions; (B) overall representation of the experimental setup.

that the temperature and pressure of the cell were not measured or controlled during the experiment and that higher temperatures were likely to occur during operation. The studied parameter settings are summarized in Table 1. Initially, the anode and cathode compartments were completely saturated with water. After homogeneous water distribution was obtained inside the anode and cathode, the water supply to the anode side was set to a constant value, as specified in Table 1; imaging with the camera was started with a frame rate of 50 fps and the potentiostat was operated galvanostatically, supplying a constant current to the system (Table 1). At the cathode side, the water flow rate was always set to a constant value of 1 ml/min to regulate the removal of produced hydrogen gas. The invasion process was monitored during steady-state operation for 180 s for each case. The voltage data was recorded simultaneously.

The stoichiometry λ in Table 1 is defined as:

$$\lambda = \frac{\dot{V}_{H_2O}^{in}}{\dot{V}_{H_2O}^{cal}}, \tag{1}$$

with

$$\dot{V}_i^{cal}\left[\frac{m^3}{s}\right] = \frac{j \cdot A}{F \cdot z} \cdot \frac{\tilde{M}}{\rho}. \tag{2}$$

In Eq. (2), for i = H$_2$O, O$_2$, $\dot{V}_i^{cal}$ denotes the volume flow rate of either oxygen or water in ml/min; F is the Faraday constant (96484 As/mol); z is the number of exchanged electrons per mole of oxygen ($z = 4$) or water ($z = 2$); $\tilde{M}$ is the molecular weight of oxygen ($32 \cdot 10^{-3}$ kg/mol) or water ($18 \cdot 10^{-3}$ kg/mol); ρ is the density at 25 °C (oxygen: 1.429 kg/m^3; water: 997.05 kg/m^3) [30]; j denotes the current density in A/cm^2, with $A = 0.5$ cm^2 being the surface area in the experimental cell.

2.3. Image processing and parameter extraction

Image processing was performed with Fiji/ImageJ 1.53c, and MATLAB 2022a was used for plotting and analysis of the data. At first, the RGB images were converted into 8-bit grey-scale images to differentiate the phases (solid, liquid, gas), as shown in Fig. 2. A median filter was used before the segmentation of images based on the Otsu threshold. The binarized images (exemplarily shown in Fig. 2B) were meshed with a 2D PN in order to determine the individual saturation of each pore and throat, as shown in Fig. 2C.

3. Results and discussions

3.1. Temporal and spatial variation of oxygen saturation

The distribution of gas and liquid in the porous electrode is commonly supposed to be relevant for the operation of the cell. The drainage and imbibition of water inside the anodic PN structure were therefore studied based on the image data captured during experiments. The binarized images (oxygen in white, water and solid in black) provide information about the temporal and local change of the overall oxygen saturation S with time, computed from:

Table 1
List of experiments and parameter settings.

Anode side water flow rate (ml/min)	Setting 1	Setting 2	Setting 3
	Current density - 0.1 A/cm^2	Current density - 1 A/cm^2	Current density - 2 A/cm^2
	Stoichiometry (λ)		
1	3558 0.71	355.87	178.25
3	10674.15	1067.61	534.75
5	17793.59	1779.35	891.26
10	35587.18	3558.71	1782.53

$$S[-] = 1 - \frac{\sum pix_{white}}{\sum pix_{total} - \sum pix_{solid}}, \tag{3}$$

with $\sum pix_{white}$ sum of white pixels, $\sum pix_{solid}$ sum of pixels referred to the solid and $\sum pix_{total}$ total number of image pixels. This is illustrated in Fig. 3. The white elements thereby represent pores and throats that contain oxygen.

The phase distributions in Fig. 3 can be read as follows. The PN at the anode was initially fully saturated with water and thus appeared completely in black at the start of the process. When oxygen was generated at the CL, it started to penetrate the PN from the bottom side. Except for setting 1, oxygen initially seemingly covered the lower side of the PN, i.e., along the CL, already at the very beginning. In setting 1, this was observed after approximately 45 s. Oxygen then started to move slowly upwards towards the water flow channel. This period is denoted as the drainage period. The velocity of the invasion front, as well as the temporal change of the overall saturation, was thereby slower at the lower current densities.

The maximum saturation was achieved when the gas phase reached the water supply channel at the top side of the PN, both in the experiment and in simulations. At this moment, part of the oxygen was quickly released, resulting in the partly re-saturation of the PN with water (Fig. 3) in experiments. This period is named the imbibition period. In contrast to drainage, imbibition of water in individual pores occurred much faster in experiments, wherefore the menisci were not developed. Only part of the pores and throats could be re-invaded by water; many pores and throats remained filled with oxygen. This phenomenon is commonly known as water starvation, e.g. Refs. [14,15]. The monitored sequences of invasion are provided as supplementary video material in **S1** (setting with 1 A/cm^2 and 1 ml/min), **S2** (1 A/cm^2 and 1 ml/min), **S3** (2 A/cm^2 and 1 ml/min), and **S4** (2 A/cm^2 and 10 ml/min).

Supplementary data related to this article can be found online at https://doi.org/10.1016/j.ijhydene.2024.06.268.

The cross-sectional view of empty channels is schematically illustrated in Fig. 4. The gas bubbles that were generated at the CL were large enough to form a continuous pathway through the PN, thereby penetrating the pores and throats completely from their lower to their upper side. As will be discussed below, water remained only in the form of thick capillary liquid films along the rough side walls of the channels.

The schematic illustration in Fig. 4, namely the full occupancy of invaded channels by the gas phase, is justified by the comparison of the theoretical oxygen evolution rate (Eq. (2)) and the generated oxygen volume computed from the image data (Fig. 5), $\dot{V}^{img}$:

$$\dot{V}^{img}\left[\frac{m^3}{s}\right] = \frac{\Delta S}{\Delta t} \cdot V_{void} \tag{4}$$

with S from Eq. (3) and V_{void} being the total pore volume of the PN. Eq. (4) supposes constant atmospheric pressure inside pores. The comparison in Fig. 5 reveals basically the same trend, i.e. increase in oxygen evolution rate with increase in current density. For a current density of 2 A/cm^2 a larger disagreement between the predictions and the measurements can be seen. This is most probably referred to the gas release via the established constant oxygen pathways, opening the transport routes between CL and FC. The continuous gas flow through the percolating routes is not captured by the image processing algorithm, as well as potential gas leakage, evaporation of water, and crossover of oxygen to the cathode.

3.2. Model-based pore-scale study of drainage

For the low oxygen flow rates and the long and wide pores and throats realized with this setup, the drainage invasion can be characterized by fully developed menisci invading several pores and throats slowly at the same time.
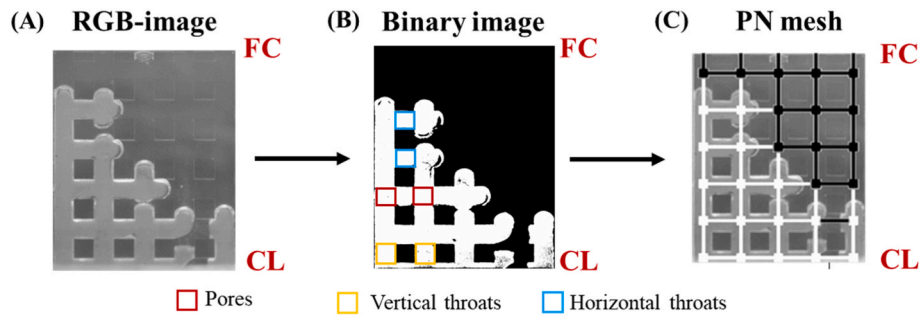
Fig. 2. (A) Original RGB-image captured during the experiment with 0.1 A/cm^2 and flow rate of 10 ml/min; solid in black, water in dark grey, and empty pores and throats in light grey. **(B)** Binarized image with oxygen pores and throats represented in white; solid and water-filled elements are represented in black. Some throats are exemplarily highlighted in blue and yellow; and some example pores, which form the throat conjunctions, are shown in red. **(C)** The PN structure was meshed to obtain individual pore and throat saturations. CL indicates the anode catalyst layer side; FC indicates the flow channel side (cf. Fig. 1). (For interpretation of the references to color in this figure legend, the reader is referred to the Web version of this article.)

The capillary number for drainage,

$$Ca = \frac{v\mu}{\sigma \cos \theta}, \tag{5}$$

with $\sigma = 0.0721$ N/m and $\mu = 9 \cdot 10^{-4}$ Pa $\cdot$ s for $T = 25\,°C$ as well as $\cos \theta \approx 1$ (the advancing contact angle is fully developed during drainage, refer to the supplementary videos **S1–S4,** ref Fig. 6A), was in the range of 10^{-5} to 10^{-6}, thus in the range of capillary invasion [20, 31–33]. In a commercial titanium felt PTL recently studied in Ref. [29], the estimated capillary number using **Eq. (5)** was Ca $= 1.08 \times 10^{-5}$ for drainage at 1.36 A/cm^2, thus in a similar range.

The invasion inside the anodic PTL was studied with two different pore-scale models (Fig. 6). LB simulations were realized with the Shen-Chen Lattice Boltzmann (SC-LB) model developed in-house, formerly presented in Refs. [28,29]. The size of the domain was 0.20×0.25 mm^2, i.e., reduced by factor 100 compared to the microfluidic PN. Initially, the domain was completely saturated water. A constant inlet velocity boundary condition near the catalyst layer was assumed, i.e., oxygen gas was injected at 15 discrete injection points along the bottom pores with a constant velocity of 0.86 mm/s, corresponding to a current density of 1 A/cm^2 and a flow rate of 1 ml/min. The simulations were carried out with Matlab (R2022a). The parameter setting used in the simulation, i. e., the pressure of $P = 1$ bar and a temperature of $T = 25\,°C$, was aligned with the experimental conditions. The results are shown in Fig. 6B, together with experimental results. Downscaling the channel width to 20 μm yielded a flat front in case of negligible pore and throat size variations, which is in excellent agreement with experiments (Fig. 6A). The liquid remaining in horizontal throats was a result of the poor 2D connectivity of the pore space, as will be further examined below.

The PN simulations were realized with the model presented in Ref. [34] as it employs viscous invasion rules. This is a specific feature that allows to invade several pores simultaneously, in line with experimental findings, based on the computation of liquid mass transport $\dot{M}_l$, using Hagen-Poisseuille equation:

$$\dot{M}_l = \frac{\rho_l \pi r^4}{8\mu L} \Delta P_l. \tag{6}$$

The simultaneous invasion is a result of the small PN realized in this work and the very small capillary pressure difference between pores and throats i and j of similar size:

$$\Delta P_c = 2 \cdot \sigma \cdot \cos \theta \left(\frac{1}{r_i} - \frac{1}{r_j} \right). \tag{7}$$

The length over which liquid could be pumped by capillarity was therefore also small. Unlike classical PN models, where the invasion of pores and throats occurs stepwise in the order of decreasing radii, the viscous PN model yielded partially saturated pores and throats, which

was in great agreement with experimental behavior (Fig. 6).

In contrast to the model in Refs. [34,35] which was originally derived to study drying, we disregarded evaporation. Instead, we computed the drainage of water based on the theoretical drainage rates from **Eq. (1)**, thereby advancing the in-house PN model from Ref. [34]. The simulations were carried out with Matlab (R2022a). The parameter setting used in the simulation was aligned with the experimental conditions, i.e. using a pressure of $P = 1$ bar, a temperature of $T = 25\,°C$ and assuming $\cos \theta \approx 1$. For the pore sizes, we anticipated a uniform channel size distribution between 2.002 mm and 2.247 mm, thereby mimicking the random variations of the microfluidic PN as expected from the manufacturing process. The volume flow rate of oxygen, computed by **Eq. (1)**, was equally distributed among the invading menisci in the viscous PN simulation. Compared to the small domain studied in Ref. [29], the cumulated inlet oxygen flow rates in this study were much greater, namely 1.139 ml/min, according to the much larger active cross-section of 0.2 cm^2. The realized gas flow rates through single pores, though, were very similar, namely varying between 0.075 mm/s and 1.4 mm/s.

Fig. 6C–i shows that the experimental phase patterns can be very well captured with the viscous PN model from Ref. [34] for the small aspect ratio of throat length to throat cross section and small variation of pore sizes. Although the studied domain size of the PTL was almost too small to differentiate between capillary fingering [36] and the formation of a flat invasion front, the PN simulations in Fig. 6C–ii clearly highlight that the order of invasion and the resulting phase patterns can be influenced by the PTL structure. The higher standard deviation of pore and throat widths in this simulation enabled liquid transport from larger to smaller pores, similarly as in Ref. [29].

Based on the results from the PN and the LB simulations, the following conclusions can be drawn for the pore-scale invasion behavior. Firstly, the high tendency of the liquid phase to remain inside horizontal throats was a result of the limited connectivity of pores and throats in the 2D structure. Secondly, the evolution of single gas fingers and the widening of the two-phase zone was clearly a result of imbibition and not of drainage. The drainage simulations rather revealed a limited expansion of the gas fingers in this roughly uniform PTL structure. Fig. 3 shows the same behavior in the very first drainage cycles of experiments. The broadening of the invasion front occurred during the first imbibition clycle, and it remained constant afterwards. Fig. 6C–ii shows that another result could be expected, if the pore and throat size distribution would be changed towards a randomly distributed structure.

As the width of the FC is in the same range as the pores in the PN (namely 4 mm wide) liquid invasion of the PTL and the FC occurs competetively. If a gas bubble is released at the right side of the channel (entrance of water, ref. Fig. 1), it can form a continuous gas pathway to the outlet of the FC and block the surface for a longer time period,
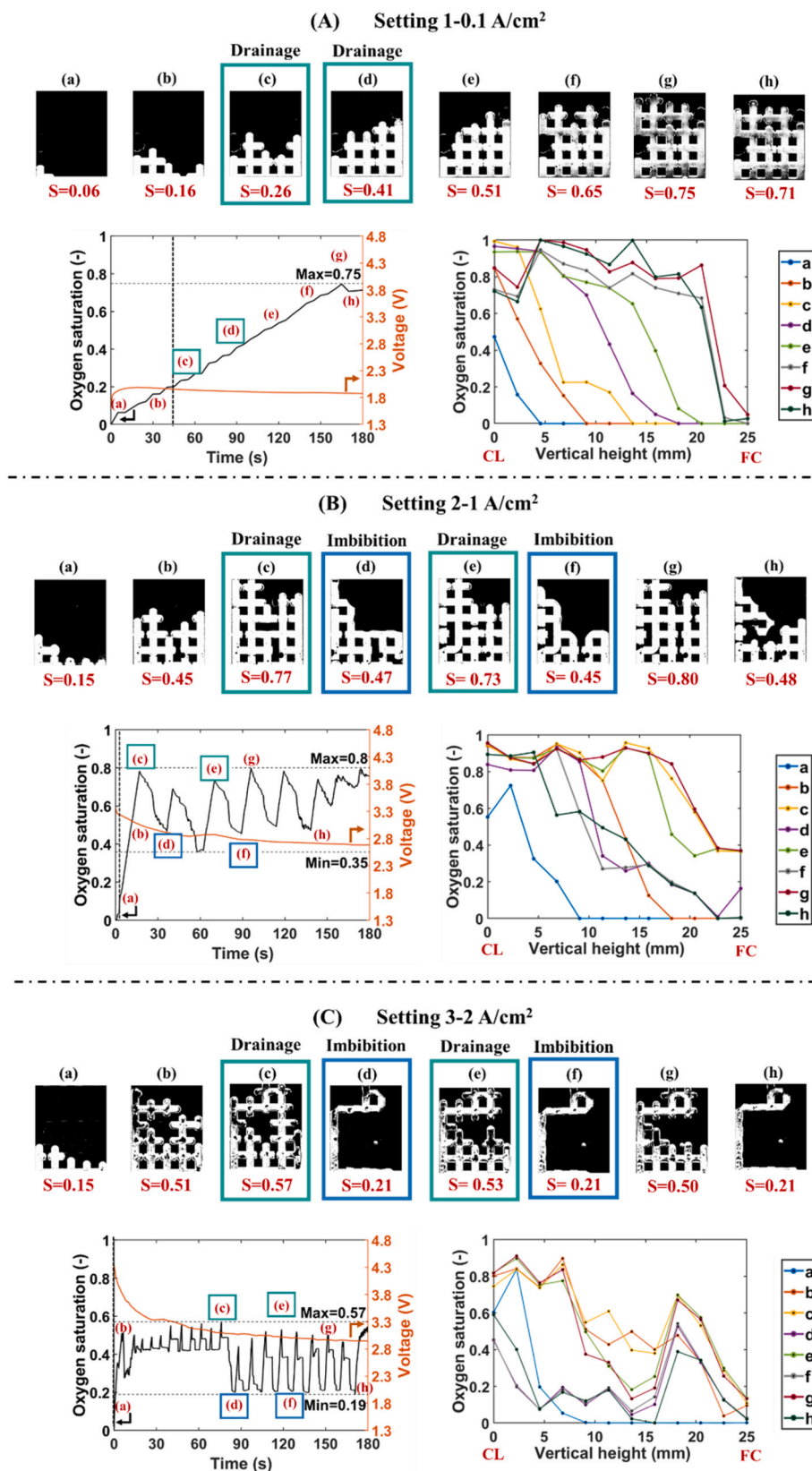
Fig. 3. Oxygen saturation with respect to time (left) and oxygen saturation profiles with respect to vertical distance (right) along with the sequence of images of the phase distributions at different time steps (top) to show the drainage and filling cycles inside the anodic PN; and corresponding voltage curves: (A) Setting 1: 0.1 A/cm² and 1 ml/min water flow rate; (B) Setting 2: 1 A/cm² and 1 ml/min; (C) Setting 3: 2 A/cm² and 10 ml/min. Filling cycle highlighted in blue and drainage cycle in green for some examples. The black vertical lines indicate the time at which the CL appeared to be covered with oxygen. This was very early in case (C). (For interpretation of the references to color in this figure legend, the reader is referred to the Web version of this article.)
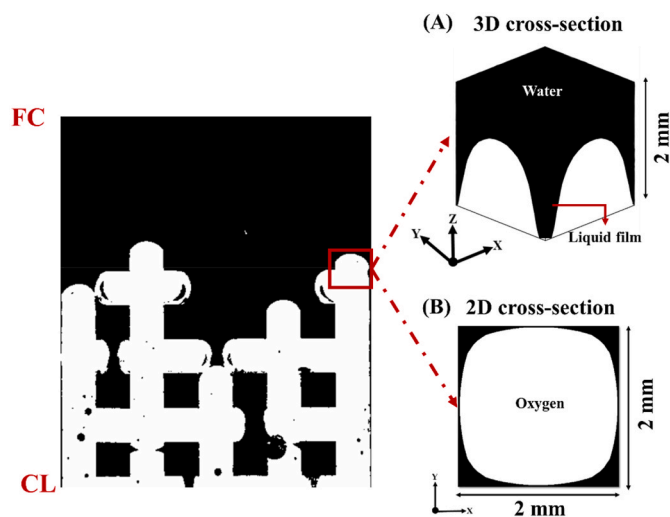
Fig. 4. Schematic illustration of drained pore and throat cross-sections.
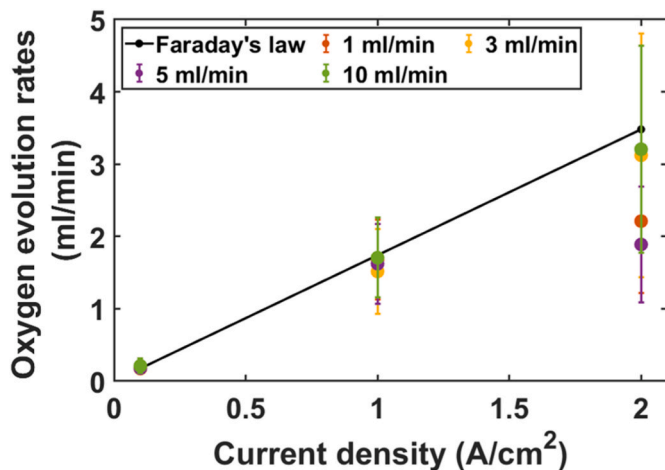

Fig. 5. Average oxygen evolution rates computed from the image data together with the theoretically computed oxygen flow rates from Faraday's law. The error bars reflect the temporal fluctuation of $\dot{V}^{img}$ in one experiment.

wherefore the gas-liquid distribution inside the PN remains unchanged. If the gas bubble is instead released at the left side (exit of water, ref. Fig. 1), it is more frequently removed (refer to supplementary material **S1** at time steps 17 s and 155 s), resulting in a higher frequency of the change of gas saturation inside the PN. This is also observed in other experimental studies, e.g. Ref. [14], and it reveals the need for a proper design of the FC [10,37].

3.3. Analysis of established oxygen invasion pathways

The phase distributions at the end of the drainage as well as at the end of the imbibition period, especially the overall gas saturations achieved after each cycle, differ from experiment to experiment. However, Fig. 3 also reveals clearly that the drainage/imbibition patterns remain almost unchanged during the same experiment. This is further revealed in Fig. 7, where the accumulated invasion events of individual pores and throats are shown for the example of experiments with setting 2 (1 A/cm² and flow rate 1 ml/min) and setting 3 (2 A/cm² and flow rate 10 ml/min). Brighter colors (i.e., white) represent a high number of drainage/imbibition cycles, whereas dark regions represent only a few invasion events. This shows that the oxygen took preferred and constant pathways through the PN in one experiment. From the PN and LB

simulations in Fig. 6 above, it can be concluded that drainage followed the pathway of least resistance, i.e. the oxygen invaded the pores and throats with lowest entry capillary pressure. In our experiment, however, where the pore and throat size variations were very small and the invasion pressure additionally influenced by the channel depth L_d,

$$P_c = \frac{\sigma \cdot r \cdot L_d}{r + L_d}, \qquad (8)$$

the invasion pathway might not have been preferentially controlled by the entry capillary pressure. Instead it is strongly assumed (based on images in Fig. 3) that the imbibition process affected the phase patterns majorly and that the flow conditions of water in the flow channel played also a significant role.

3.4. Investigation of secondary transport mechanisms

Most interestingly, the voltage curves provided in Fig. 3 did not follow the frequency of the oxygen invasion profiles. Oxygen seemingly covered the CL interface located at the bottom side of the images already at the start of each experiment, cf. also Fig. 4. This is also illustrated by the spatially resolved saturation profiles in Fig. 3. This observation is unique in all experiments. According to the stoichiometry of the OER, the water flow rate to the CCM must have been at least $2.8 \cdot 10^{-3}$ ml/min for a current density of 1 A/cm² to sustain the reaction rate. The question evolves, how the CL could be supplied with water after the oxygen apparently covered the CL interface. There are two possible explanations: i) water from the cathode side penetrated the membrane to the anode side (refer e.g. to supplementary material **S3** at time step 10–20 s at bottom side, right near to CL) [38,39]; ii) wetting liquid films occurred inside the PN structure of the anode. The latter situation is analyzed in Fig. 8. Instead of flooding the cathode with water, it was kept dry in the test experiment. Oxygen also covered immediately the CL interface, while the OER was sustained (Fig. 8A), as in all other experiments. This shows that water crossover might have played a minor role in our experiments and that rather wetting liquid films could be a reasonable explanation. In more details, thick capillary liquid films are expected to have covered the rough inner walls of the microfluidic PTL (as illustrated in Fig. 4) while the oxygen penetrated through the bulk pore space. This phenomenon was a result of the wetting of water along the rough wall surfaces and sharp pore corners. Such films were also observed in previous works, e.g. Refs. [27,40].

It is anticipated that these films formed a continuous pathway along the lateral walls (Fig. 8B). Their liquid permeability in the given PN structure can be calculated in dependence of their thickness, assuming that it is constant throughout the PN and that the films are continuous, i. e. ignoring the exact position of liquid menisci and assuming that each throat contains liquid films of identical width (Fig. 8B). The liquid permeability of the PN with an approximate porosity of $\varepsilon \simeq 0.82$ is $K = 3.35 \cdot 10^{-8}$ if it is completely water saturated. The anticipated film thickness based on image data is approximately 250 μm. The required liquid volume flow rates at the given current densities of 0.1 A/cm², 1 A/cm² and 2 A/cm² are low, namely between $2.8 \cdot 10^{-4}$ and $5.61 \cdot 10^{-3}$ ml/min according to Eq. (1). This flow rate is expected to be sustained by liquid films of 250 μm thickness along the PN even if the liquid pressure gradient between the advancing menisci and the FC is small.

In experiments with flooded cathode, both, liquid films and water permeation through the membrane might have sustained water supply after oxygen coverage of the CL. This outcome leads to the conclusion that mass transfer kinetics might benefit from secondary water transport mechanisms although a direct comparison with a reference case without such an effect is at the moment not possible.

It is noted that major focus of this study is not on the electrochemical performance of the model cell but on the invasion of the PN with oxygen and water. However, the results indicate that the presence of liquid water on the cathode side could contribute to an increase in the mass
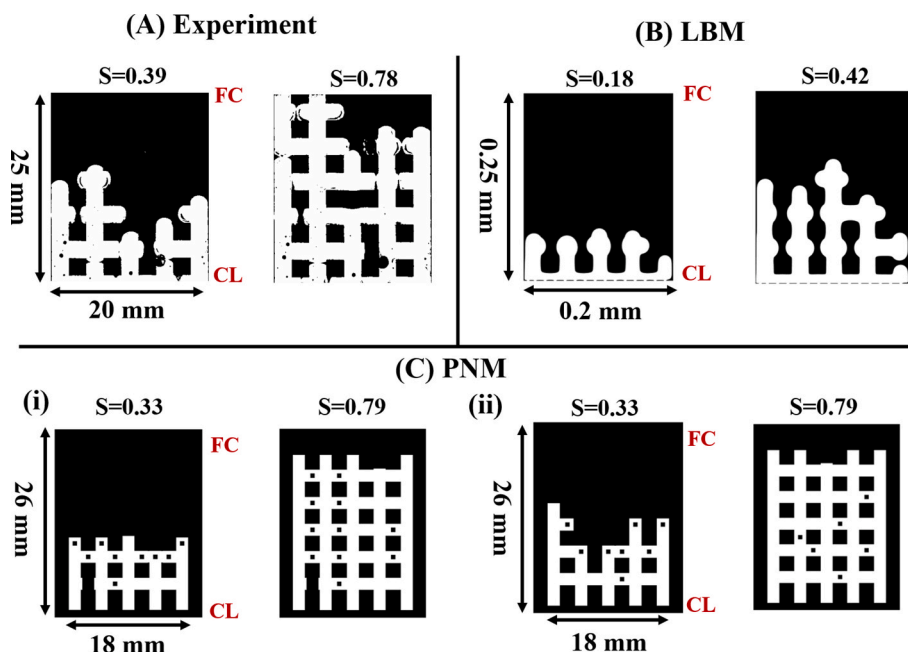
Fig. 6. PN and LB simulation results in comparison to experimental images. The background and water-saturated pores and throats are shown in black and empty elements in white. Phase patterns obtained from: (A) experiments with $j = 1$ A/cm^2 and water flow rate of 1 ml/min; (B) LB simulations for domain size reduced by a factor of 100 compared to experimental PN structure and $j = 1$ A/cm^2 and water flow rate of 1 ml/min (C - i) PN simulations with structure identical to experiment; (C – ii) PN with a higher variation of pore and throat widths (normalized distributed throat width 2 ± 0.9 mm, channel depth equal to throat width and $j = 0.1$ A/cm^2. Partially filled throats are identified by a small black rectangle in the center of PN simulations.
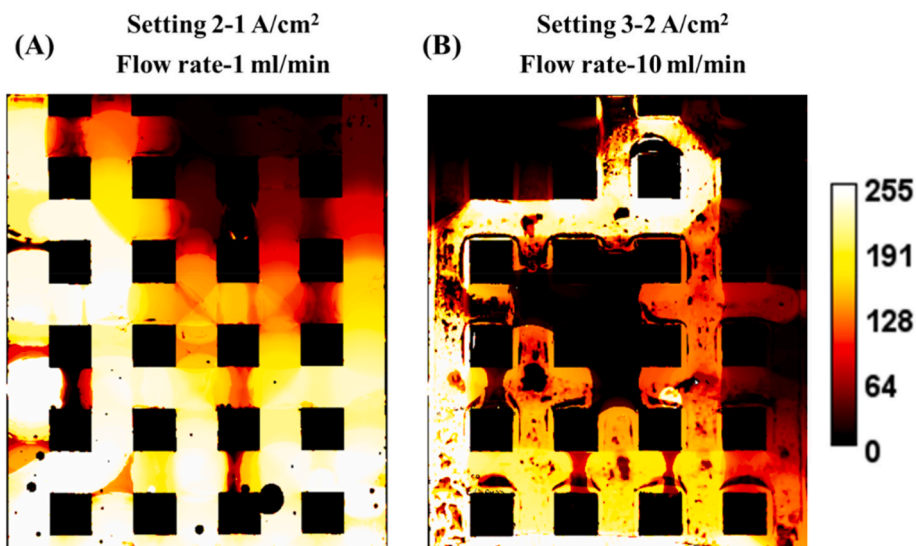

Fig. 7. Accumulated phase patterns, showing that the gas pathways remained roughly constant and that re-invasion by water occurred in almost identical pores in (A) setting 2 (1 A/cm^2; flow rate 1 ml/min) and (B) setting 3 (2 A/cm^2; 10 ml/min). The brighter color refers to a higher number of invasions. The black regions were never invaded during the experiment. (For interpretation of the references to color in this figure legend, the reader is referred to the Web version of this article.)

transport resistance at the cathode and, thus, to an increase in the overall voltage (Fig. 3 and **S5**). This was also confirmed in an experiment in which the cathode was operated without liquid water (Fig. 8), where a lower voltage was observed.

In addition to that, the temperature was not monitored or controlled during experiments. It is likely that temperature increased during the experiment due to the low heat conductivity of PMMA as well as potential (i.e. electrochemical) losses in the cell. It can be speculated that the primary as well as the secondary water transfer routes, i.e. through bulk channels, through the membrane, and through liquid films, were interrupted at higher temperatures due to the associated evaporation of

water and the dry out of the transport pathway. In more detail, evaporation of water in the bulk liquid phase and in liquid films could potentially result in the split-up of the liquid phase into single and isolated clusters, which, from this moment, would not contribute to the liquid transport between FC and CL anymore and which could be an additional source of potential losses.

3.5. Dependence of phase patterns on process parameters

The data presented in Fig. 9 is averaged from the drainage-filling periods of all experiments. Fig. 9 suggests that the frequency and
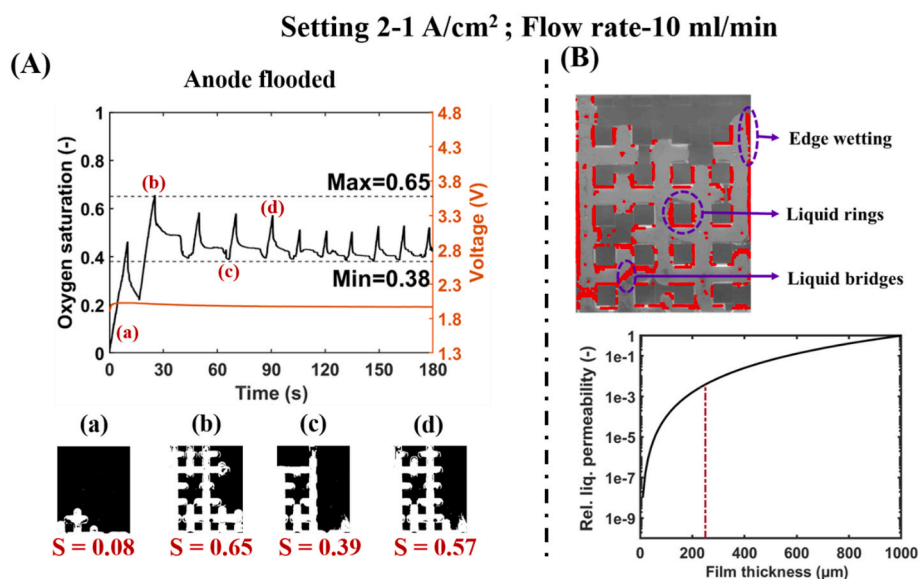
Fig. 8. (A) Test experiment with dry cathode and water flooded only at the anode side. (B) Visualization of liquid films (top, in red) and permeability of liquid films in dependence of their thickness, assuming complete coverage and constant film thickness throughout the PN (bottom). (For interpretation of the references to color in this figure legend, the reader is referred to the Web version of this article.)
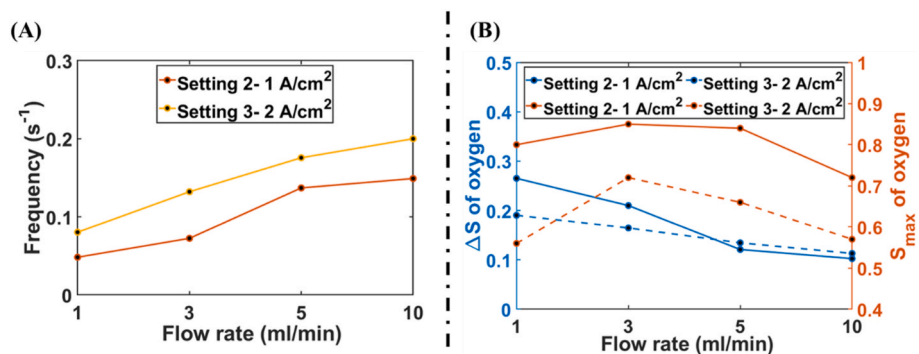

Fig. 9. (A) Dependence of the frequency of drainage/imbibition cycles on water flow rates and current density; (B) maximum saturation and amplitude of ΔS.

amplitude of the change in oxygen saturation depend on the current density and water flow rates. Only in the case of setting 1 (not shown in Fig. 9) the oxygen evolution rates were generally too low to allow for several cycles in the given time frame of 180 s. The repeatability of experiments though was very good in case of setting 1 and all flow rates (in total 3 repetitions), namely: the maximum oxygen saturation achieved in the first drainage cycle was $S = 0.69 \pm 0.06$, 0.55 ± 0.04, 0.63 ± 0.05, 0.56 ± 0.07, respectively; the time to complete the first drainage cycle was $t = 165 \pm 5$ s, 140 ± 10 s, 140 ± 10 s, 135 ± 5 s, 120 ± 5 s. Both variables revealed a low standard deviation.

For a current density of 1 A/cm^2 the repeatability was also good, reflected by the small standard deviation of the maximum saturation achieved during the imbibition-drainage cycles, which was $S = 0.76 \pm 0.04$ s, 0.81 ± 0.03 s, 0.77 ± 0.06 s, 0.79 ± 0.07 (after 3 repetitions with this parameter setting). In case of 2 A/cm^2 the experimental procedure was very difficult, explained with the previously mentioned effects (cf. discussions related to temperature increase and water evaporation in **Section 3.4**). The experiments could, therefore not be repeated with the same reliability as in the other situations, and the obtained results spread much more, which is not reflected by Fig. 9. However, the periodic change of imbibition and drainage was well evolved in the case of 2 A/cm^2, too, whereas in the case of 1 A/cm^2 the profiles are not well recognized (refer to Fig. S5 in supplementary material).

4. Conclusions

In this study, we presented a novel concept of a microfluidic PEM water electrolyzer cell to investigate the counter-current two-phase flow at the structured anode PTL using an experimental setup with a potentiostat, a digital camera, and supplementary data from pore-scale PN and LB simulations.

Analysis of the water and oxygen phase distributions inside the PN structure of the anode compartment revealed that invasion occurred in alternating drainage/imbibition cycles. Drainage of water by the gas phase was thereby controlled by the OER, with fully evolved liquid menisci moving relatively slowly through the PN. Due to the low variation of pore and throat sizes the effect of capillary fingering could not be demonstrated. The water imbibition process instead was very fast and the PN was never completely re-saturated by water during the imbibition periods. Instead, a rather fractal phase distribution developed after each imbibition cycle. An average quasi-steady state was achieved, around which the oxygen saturation decreased and increased in repeated drainage/imbibition cycles with almost constant frequency. Moreover, the oxygen took preferential pathways during these cycles, which were speculated to depend on the imbibition process and potentially additionally on the water flow conditions in the flow channel.

As the voltage curve remained stable during these cycles, we

considered secondary transport pathways as a key for water supply to the CL. It was anticipated that the water could pass the membrane from the water-flooded cathode side and travelled through interconnected thick wetting liquid films of up to 250 μm width.

Although the first outcomes show that in general the dynamics of the invasion process can be studied with such a setup, the electrochemical performance of the model cell can still be improved. Especially at the higher current density of 2 A/cm^2, the experimental procedure was very difficult and also affected, e.g., by water starvation. In order to study additionally the dependence of invasion patterns on pore-size variations, the PN could perspectively be replaced by structures as used in e.g. Refs. [22,23].

Declaration of competing interest

The authors declare that they have no known competing financial interests or personal relationships that could have appeared to influence the work reported in this paper.

CRediT authorship contribution statement

Supriya Bhaskaran: Conceptualization, Data curation, Formal analysis, Investigation, Methodology, Software, Validation, Visualization, Writing – original draft. **Tamara Miličić:** Data curation, Formal analysis, Methodology, Writing – review & editing. **Tanja Vidaković-Koch:** Formal analysis, Project administration, Resources, Supervision, Writing – review & editing. **Vikranth Kumar Surasani:** Resources, Supervision, Writing – review & editing. **Evangelos Tsotsas:** Project administration, Resources, Supervision, Writing – review & editing. **Nicole Vorhauer-Huget:** Conceptualization, Funding acquisition, Methodology, Project administration, Resources, Software, Supervision, Validation, Visualization, Writing – review & editing.

Acknowledgments

Appendix A. Supplementary data

Supplementary data to this article can be found online at https://doi.org/10.1016/j.ijhydene.2024.06.268.

List of symbols

Nomenclature

A	Cross-sectional area (cm^2)
Ca	Capillary number (−)
I	Current (A)
j	Current density (A cm^{-2})
E_{cell}^0	Thermodynamic cell voltage (V)
F	Faraday constant (A s mol^{-1})
fps	Frame rates per second (s^{-1})
k	Relative Permeability (−)
K	Absolute permeability (m^2)
L	Length
$\dot{M}$	Mass flow rate (kg s^{-1})
$\tilde{M}$	Molecular weight (g mol^{-1})
P	Pressure (Pa)
pix	Pixels
$\tilde{R}$	Ideal gas constant (J kmol^{-1} K^{-1})
r	Radius
S	Saturation
T	Temperature (K)
t	Time (s)
v	Velocity (mm/s)
V	Volume (m^3)
$\dot{V}$	Volume flow rate (ml min^{-1})

Greek letters

μ	Dynamic viscosity (Pa s)
ρ	Macroscopic density (kg m^3)
ε	Porosity (−)
λ	Stoichiometry (−)
σ	Surface tension (N m^{-1})

Subscripts/Superscripts

black	Black pixels
c	capillary

cal	Calculated
d	Depth
eq	Equilibrium
img	Image
O_2	Oxygen
solid	Solid pixels
total	Total pixels
void	Void
H_2O	Water

Abbreviation

CL	Catalyst layer
FC	Flow channel
HFR	High-frequency resistance
LB	Lattice Boltzmann
OER	Oxygen evolution reaction
PN	Pore network
PEMWE	Polymer electrolyte membrane water electrolyzer
PTL	Porous transport layer

References

[1] Nikolaidis P, Poullikkas A. A comparative overview of hydrogen production processes. Renew Sustain Energy Rev 2017;67:597–611. https://doi.org/10.1016/j.rser.2016.09.044.

[2] Grigoriev SA, Porembsky VI, Fateev VN. Pure hydrogen production by PEM electrolysis for hydrogen energy. Int J Hydrogen Energy 2006;31:171–5. https://doi.org/10.1016/j.ijhydene.2005.04.038.

[3] Shiva Kumar S, Himabindu V. Hydrogen production by PEM water electrolysis – a review. Mater Sci Energy Technol 2019;2:442–54. https://doi.org/10.1016/j.mset.2019.03.002.

[4] Selamet OF, Pasaogullari U, Spernjak D, Hussey DS, Jacobson DL, Mat M. In situ two-phase flow investigation of proton exchange membrane (PEM) electrolyzer by simultaneous optical and neutron imaging. ECS Trans 2011;41:349–62. https://doi.org/10.1149/1.3635568.

[5] Siracusano S, Di Blasi A, Baglio V, Brunaccini G, Briguglio N, Stassi A, et al. Optimization of components and assembling in a PEM electrolyzer stack. Int J Hydrogen Energy 2011;36:3333–9. https://doi.org/10.1016/j.ijhydene.2010.12.044.

[6] Suermann M, Takanohashi K, Lamibrac A, Schmidt TJ, Büchi FN. Influence of operating conditions and material properties on the mass transport losses of polymer electrolyte water electrolysis. J Electrochem Soc 2017;164:F973–80. https://doi.org/10.1149/2.13517109jes.

[7] Schuler T, Schmidt TJ, Büchi FN. Polymer electrolyte water electrolysis: Correlating performance and porous transport layer structure: Part II. Electrochemical performance analysis. J Electrochem Soc 2019;166:F555–65. https://doi.org/10.1149/2.1241908jes.

[8] Majasan JO, Iacoviello F, Cho JIS, Maier M, Lu X, Neville TP, et al. Correlative study of microstructure and performance for porous transport layers in polymer electrolyte membrane water electrolysers by X-ray computed tomography and electrochemical characterization. Int J Hydrogen Energy 2019;44:19519–32. https://doi.org/10.1016/j.ijhydene.2019.05.222.

[9] Majasan JO, Iacoviello F, Shearing PR, Brett DJL. Effect of microstructure of porous transport layer on performance in polymer electrolyte membrane water electrolyser. Energy Proc 2018;151:111–9. https://doi.org/10.1016/j.egypro.2018.09.035.

[10] Majasan JO, Cho JIS, Dedigama I, Tsaoulidis D, Shearing P, Brett DJL. Two-phase flow behaviour and performance of polymer electrolyte membrane electrolysers: electrochemical and optical characterisation. Int J Hydrogen Energy 2018;43:15659–72. https://doi.org/10.1016/j.ijhydene.2018.07.003.

[11] Zielke L, Fallisch A, Paust N, Zengerle R, Thiele S. Tomography based screening of flow field/current collector combinations for PEM water electrolysis. RSC Adv 2014;4:58888–94. https://doi.org/10.1039/c4ra12402b.

[12] Ito H, Maeda T, Nakano A, Hwang CM, Ishida M, Kato A, et al. Experimental study on porous current collectors of PEM electrolyzers. Int J Hydrogen Energy 2012;37:7418–28. https://doi.org/10.1016/j.ijhydene.2012.01.095.

[13] Ito H, Maeda T, Nakano A, Kato A, Yoshida T. Influence of pore structural properties of current collectors on the performance of proton exchange membrane electrolyzer. Electrochim Acta 2013;100:242–8. https://doi.org/10.1016/j.electacta.2012.05.068.

[14] Panchenko O, Borgardt E, Zwaygardt W, Hackemüller FJ, Bram M, Kardjilov N, et al. In-situ two-phase flow investigation of different porous transport layer for a polymer electrolyte membrane (PEM) electrolyzer with neutron spectroscopy. J Power Sources 2018;390:108–15. https://doi.org/10.1016/j.jpowsour.2018.04.044.

[15] Altaf H, Milicic T, Vidakovic-Koch T, Tsotsas E, Tengattini A, Kardjilov N, et al. Neutron imaging experiments to study mass transport in commercial titanium felt porous transport layers. J Electrochem Soc 2023;170:064507. https://doi.org/10.1149/1945-7111/acd7a8.

[16] Maier M, Dodwell J, Ziesche R, Tan C, Heenan T, Majasan J, et al. Mass transport in polymer electrolyte membrane water electrolyser liquid-gas diffusion layers: a combined neutron imaging and X-ray computed tomography study. J Power Sources 2020;455. https://doi.org/10.1016/j.jpowsour.2020.227968.

[17] Seweryn J, Biesdorf J, Schmidt TJ, Boillat P. Communication—neutron radiography of the water/gas distribution in the porous layers of an operating electrolyser. J Electrochem Soc 2016;163:F3009–11. https://doi.org/10.1149/2.0641607jes.

[18] Lee JK, Lee CH, Fahy KF, Zhao B, LaManna JM, Baltic E, et al. Critical current density as a performance indicator for gas-evolving electrochemical devices. Cell Reports Phys Sci 2020;1:100147. https://doi.org/10.1016/j.xcrp.2020.100147.

[19] Lee CH, Lee JK, George MG, Fahy KF, LaManna JM, Baltic E, et al. Reconciling temperature-dependent factors affecting mass transport losses in polymer electrolyte membrane electrolyzers. Energy Convers Manag 2020;213. https://doi.org/10.1016/j.enconman.2020.112797.

[20] Zlobinski M, Schuler T, Büchi FN, Schmidt TJ, Boillat P. Transient and steady state two-phase flow in anodic porous transport layer of proton exchange membrane water electrolyzer. J Electrochem Soc 2020;167:084509. https://doi.org/10.1149/1945-7111/ab8c89.

[21] Satjaritanun P, O'Brien M, Kulkarni D, Shimpalee S, Capuano C, Ayers KE, et al. Observation of preferential pathways for oxygen removal through porous transport layers of polymer electrolyte water electrolyzers. iScience 2020;23:101783.

[22] Arbabi F, Kalantarian A, Abouatallah R, Wang R, Wallace JS, Bazylak A. Feasibility study of using microfluidic platforms for visualizing bubble flows in electrolyzer gas diffusion layers. J Power Sources 2014;258:142–9. https://doi.org/10.1016/j.jpowsour.2014.02.042.

[23] Lee CH, Hinebaugh J, Banerjee R, Chevalier S, Abouatallah R, Wang R, et al. Influence of limiting throat and flow regime on oxygen bubble saturation of polymer electrolyte membrane electrolyzer porous transport layers. Int J Hydrogen Energy 2017;42:2724–35. https://doi.org/10.1016/j.ijhydene.2016.09.114.

[24] Litster S, Sinton D, Djilali N. Ex situ visualization of liquid water transport in PEM fuel cell gas diffusion layers. J Power Sources 2006;154:95–105. https://doi.org/10.1016/j.jpowsour.2005.03.199.

[25] Altaf H, Vorhauer N, Tsotsas E, Vidaković-Koch T. Steady-state water drainage by oxygen in anodic porous transport layer of electrolyzers: a 2D pore network study. Processes 2020;8. https://doi.org/10.3390/PR8030362.

[26] Vorhauer-Huget N, Altaf H, Dürr R, Tsotsas E, Vidaković-Koch T. Computational optimization of porous structures for electrochemical processes. Processes 2020;8. https://doi.org/10.3390/PR8101205.

[27] Vorhauer N, Wang YJ, Kharaghani A, Tsotsas E, Prat M. Drying with formation of capillary rings in a model porous medium. Transport Porous Media 2015;110:197–223. https://doi.org/10.1007/s11242-015-0538-1.

[28] Paliwal S, Panda D, Bhaskaran S, Vorhauer-Huget N, Tsotsas E, Surasani VK. Lattice Boltzmann method to study the water-oxygen distributions in porous transport layer (PTL) of polymer electrolyte membrane (PEM) electrolyser. Int J Hydrogen Energy 2021;46:22747–62. https://doi.org/10.1016/j.ijhydene.2021.04.112.

[29] Bhaskaran S, Pandey D, Surasani VK, Tsotsas E, Vidakovic-Koch T, Vorhauer-Huget N. LBM studies at pore scale for graded anodic porous transport layer (PTL) of PEM water electrolyzer. Int J Hydrogen Energy 2022;47:31551–65. https://doi.org/10.1016/j.ijhydene.2022.07.079.

[30] Green DW, Southard MZ, editors. Perry's chemical engineers' handbook. ninth ed. New York: McGraw-Hill Education; 2019.

[31] Lenormand R. Flow through porous media: limits of fractal patterns. Proc R Soc London A Math Phys Sci 1989;423:159–68. https://doi.org/10.1098/rspa.1989.0048.

[32] Lenormand R. Liquids in porous media. J Phys Condens Matter 1990;2. https://doi.org/10.1088/0953-8984/2/S/008.

[33] Zacharoudiou I, Boek ES, Crawshaw J. Pore-scale modeling of drainage displacement patterns in association with geological sequestration of CO2. Water Resour Res 2020;56:1–20. https://doi.org/10.1029/2019WR026332.

[34] Metzger T, Tsotsas E. Viscous stabilization of drying front: three-dimensional pore network simulations. Chem Eng Res Des 2008;86:739–44. https://doi.org/10.1016/j.cherd.2008.03.003.

[35] Metzger T, Vu TH, Irawan A, Surasani VK, Tsotsas E. Pore-scale modelling of transport phenomena in drying. https://doi.org/10.1007/978-3-540-85715-0_15; 2008.

[36] Vorhauer N, Altaf H, Tsotsas E, Vidakovic-Koch T. Pore network simulation of gas-liquid distribution in porous transport layers. Processes 2019;7. https://doi.org/10.3390/pr7090558.

[37] Roenning FH, Roy A, Aaron DS, Mench MM. Mass transport limitations in polymer electrolyte water electrolyzers using spatially-resolved current measurement. J Power Sources 2022;542:231749. https://doi.org/10.1016/j.jpowsour.2022.231749.

[38] Watanabe M, Satoh Y, Shimura C. Management of the water content in polymer electrolyte membranes with porous fiber wicks. J Electrochem Soc 1993;140: 3190–3. https://doi.org/10.1149/1.2221008.

[39] Schalenbach M, Carmo M, Fritz DL, Mergel J, Stolten D. Pressurized PEM water electrolysis: efficiency and gas crossover. Int J Hydrogen Energy 2013;38: 14921–33. https://doi.org/10.1016/j.ijhydene.2013.09.013.

[40] Bhaskaran S, Pandey D, Panda D, Paliwal S, Vorhauer N, Tsotsas E, et al. Study on film effects during isothermal drying of square capillary tube using Lattice Boltzmann method. Dry Technol 2022;40:735–47. https://doi.org/10.1080/07373937.2021.1898417.